

submitted to ApJ, July 9, 2009

# Metal-Enriched Outflows in the Ultra-Luminous infrared Quasar Q1321+058

Tinggui Wang<sup>1,2</sup>, Hongyan Zhou<sup>3,1,2</sup>, Weimin Yuan<sup>4</sup>, HongLin Lu<sup>2</sup>, Xiaobo Dong<sup>1,2</sup> and  
Hongguang Shan<sup>4</sup>

*CAS Key Laboratory for Research in Galaxies and Cosmology, University of Science and  
Technology of China, Hefei, Anhui, 230026, P.R.China*

*Center for Astrophysics, University of Science and Technology of China, Hefei, Anhui,  
230026, P.R. China*

*Department of Astronomy, University of Florida, Gainesville, FL 32611*

*Yunnan Astronomical Observatory, National Astronomical Observatories, Chinese  
Academy of Sciences, P.O. Box 110, Kunming, Yunnan 650011, China*

## ABSTRACT

Quasar outflows may play important role in the evolution of its host galaxy and central black hole, and are most often studied in absorption lines. In this paper, we present a detailed study of multiple outflows in the obscured ultra-luminous infrared quasar Q1321+058. The outflows reveal themselves in the complex optical and UV emission line spectrum, with a broad component blueshifted by  $1650 \text{ km s}^{-1}$  and a narrow component by  $360 \text{ km s}^{-1}$ , respectively. The higher velocity component shows ever strong N III] ( $\text{N III]}/\text{C III]} = 3.8 \pm 0.3$  and  $\text{N III]}/\text{C IV} = 0.53$ ) and strong Si III] ( $\text{Si III]}/\text{C III]} \simeq 1$ ), in addition to strong  $[\text{O III}]\lambda 5007$  and  $[\text{Ne III}]\lambda 3869$  emission. A comparison of these line ratios with photoionization models suggests an overabundance of N and Si relative to C. The abundance pattern is consistent a fast chemical enriching process associated with a recent starburst, triggered by a recent galaxy merger. The outflow extends to several tens to hundred parsecs from the quasar, and covers only a very small sky. We find that the outflow with line emitting gas is energetically insufficient to remove the ISM of the host galaxy, but total kinetic energy may be much larger than suggested by the emission lines. The velocity range and the column density suggest that the outflow might be part of the low ionization broad absorption line region as seen in a small class of quasars.

The optical and UV continuum is starlight-dominated and can be modeled with a young-aged (1 Myr) plus an intermediate-aged ( $\sim 0.5 - 1$  Gyr) stellar populations, suggesting a fast building of the stellar mass in the host galaxy, consistent with the starburst-type metal abundances inferred from the high velocity outflow spectrum. The broad band spectral energy distribution shows that it is an obscured quasar with its bulk emission in the middle infrared. The star formation rate, independently estimated from UV, far-infrared, and emission line luminosity, is much lower than that is required for the co-evolution of the black hole and its host spheroid.

*Subject headings:* galaxies:individual–galaxies:nuclei–quasars:emission lines–galaxies:starburst

## 1. Introduction

A consensus is now forming that quasar activities are triggered through mergers of gas-rich massive galaxies. The evidence accumulated in the past decade includes the presence of tidal tails in their host galaxies (e.g. Kirhakos et al. 1999 ; Hutchings et al. 1999 ), and signatures of a recent starburst in the off-nuclear spectrum (e.g. Canalizo & Stockton 2000a; Canalizo & Stockton 2000b) and in the composite spectrum of less luminous AGN (e.g. Heckman et al. 2004 ; Vanden Berk et al. 2006 ). The merger of gas-rich galaxies also leads to starburst in the nuclear as well as outskirt regions. As such, most of these systems appear as luminous or ultra-luminous infrared galaxies ( $L_{ir} > 10^{12} L_{\odot}$ , ULIRGs). The connection between ULIRGs and quasars has been widely discussed, and there is evidence for an evolution sequence between the two (e.g. Sanders & Mirabel 1996 ; Zheng et al. 1999 ).

Vigorous starburst and nuclear activity will result in a strong negative feedback to the host galaxy. Massive winds have been observed in starburst galaxies, ULIRG and AGN with mass outflow rates from 10 to 1000  $M_{\odot} \text{ yr}^{-1}$  (e.g. Rupke et al. 2005 ; Lípari et al. 2005 ). It was proposed that such a feedback will quench gas supply to the AGN and the star-formation region, and result in a sudden halt of the star-formation process in the galaxies (e.g. Di Matteo et al. 2005 ). The passively evolved galaxies will first appear as E+A in the subsequent  $\sim 1$  Gyr, and then as red galaxies. The latter can explain the red colors of massive early type galaxies (Springel et al. 2005 ). If quasar activity is going-on for sometime after the star-formation essentially ceased, the object will show characteristics of Q+A. Q+A's have been detected now with a large number in the Sloan Digital Sky Survey (York et al. 2000 , SDSS). Most of these systems show weak [O II] emission, likely from the Narrow Line Region (NLR), indicating that major star-forming activity has ceased (Zhou et al. 2005 ), or, at least, is greatly suppressed. Indeed, Ho (2005) found that

the ratio of SFR to mass accretion rate in PG quasars is well below that required for sustaining the  $M_{BH} - \sigma$  relation for nearby spheroid galaxies. It was further suggested that this is due to that star formation is suppressed rather than that cold gas is exhausted. It should be noted that the author used the [O II] emission-line luminosity to infer SFR, for which the reddening correction is largely uncertain, however.

Gas outflows are thought to play an important role in the galactic scale feedback. Outflows on scales of tens to hundreds parsecs have been observed in nearby Seyfert galaxies and radio galaxies with velocities of a few hundreds to thousand  $\text{km s}^{-1}$  (e.g. Gabel et al. 2005 ; Das et al. 2005 ; Ruiz et al. 2005 ). However, modeling the absorption and emission lines for well-studied nearby Seyfert galaxies suggested a relative low mass loss rate and small kinetic power in these outflows (Crenshaw, Kraemer & George 2003). Even higher velocity outflows, from a few  $10^3$  to  $10^4 \text{ km s}^{-1}$ , are detected in broad absorption line (BAL) quasars (e.g. Weymann et al. 1991 ), but the scale and the total mass in BAL outflows are still not clear, neither the relation between the BAL region (BALR) and the narrow/broad emission-line region (N/BELR).

The recent intensive starburst in the circum-nuclear region has also significant implications for the gas phase metallicity. Massive stars evolve very fast and produce a chemical pollution in the circum-nuclear ISM primarily with  $\alpha$ -elements via SN II, while less massive stars evolve much slowly and make their chemical contribution of iron peaked elements, mainly through SNIa, with a delay of at least 1 Gyr. The detail abundance pattern depends on both the history of star-formation and the stellar initial mass function. Supersolar metallicity has been suggested by analyzing the broad line and broad absorption line spectra (e.g., Hamann 1997; Baldwin et al. 2003) , which are produced in a relative small region enclosed the active nucleus. However, it is still not clear whether this reflects an over-all high metallicity or only these elements concerned.

In this paper, we study in detail the optical and ultraviolet (UV) spectra and the broad band properties of the ULIRG Q 1321+058. This object was classified as a quasar based on a low resolution spectrum taken in the optical identification processes of HEAO 1-A2 (The High Energy Astrophysics Observatory-1) X-ray sources (Remillard et al. 1993 ). However, it was not detected by XMM-Newton (Bianchi et al. 2005), which led these authors to propose that it is a Compton-thick, type II object. The optical image taken with Hubble Space Telescope (HST) showed a strong disturbed morphology possibly with a double nucleus of separation less than 1 kpc, suggesting a recent merger of two gas-rich galaxies (Boyce et al. 1996). Darling & Giovanelli (2002) detected an OH Megmaser with a multi-peaked profile, which they interpreted as possible multiple maser nuclei. Here we show that its broad band properties are consistent with an obscured quasar. The optical and the

UV continuum is likely dominated by starlight, that is also typical for a type II object. Extreme velocity outflows (EVOFs) were noticed previously in the [O III] and H $\beta$  emission-lines (Lípari et al. 2003 ). Taking the advantage of the broad wavelength coverage of the SDSS spectrograph, we have identified the EVOFs in H $\alpha$  and [Ne III] $\lambda$ 3869. We find that the EVOFs also appear in the UV lines in the HST (Hubble Space Telescope) FOS spectrum, such as C IV $\lambda$ 1549, N III] $\lambda$ 1750, Al III] $\lambda$ 1860, Si III] $\lambda$ 1892, and C III] $\lambda$ 1909. The line ratios imply a dense line emitting gas with a fast metal enriched history. We find with interest that the velocity range and the column density of the AGN-driven outflows are comparable to those in low-ionization BALR (LoBALR), implying that the object would appear as a LoBAL quasar if our line-of-sight passing through the outflows. These unusual properties of Q 1321+058 provides us with an ideal laboratory to study the impact of AGN and starburst feed-backs to galaxy formation and evolution. Throughout this paper, we assume a  $\Lambda$ -CDM cosmology with  $H_0 = 72 \text{ km s}^{-1} \text{ Mpc}^{-1}$ ,  $\Omega_\Lambda = 0.7$  and  $\Omega_m = 0.3$ .

## 2. Modeling Continuum and Emission Line

The SDSS spectrum used in this work was extracted from the SDSS archive<sup>1</sup>. The UV spectrum was observed with the high-resolution gratings of the Faint Object Spectrograph (FOS) on board HST (Bechtold et al. 2002). We retrieved the calibrated 1-D spectrum from the HST archive using the on-flight calibration. The spectra of two exposures are combined to remove cosmic rays. Both optical and UV spectra are wavelength- and flux-calibrated. The spectra are corrected for Galactic reddening of E(B-V)=0.031 (Schlegel et al. 1998 ) and are shifted into the rest frame of the object using a redshift of  $z = 0.20467$  as measured from optical emission lines (see below).

### 2.1. Continuum

The optical continuum shows prominent high order Balmer absorption lines, thus is likely dominated by starlight (Fig 1). We model the continuum with the templates derived using the ICA method (refer to Lu et al. (2006) for detail) assuming no contribution from the AGN:

$$f(\lambda) = A(\lambda) \sum a_i I C_i(\lambda) \quad (1)$$

---

<sup>1</sup><http://www.sdss.org/>.

where  $A(\lambda)$  is the dust extinction factor,  $IC_i$  the  $i$ th independent component. Note that both  $IC_i$  and  $a_i$  are positive. The intrinsic reddening is taken as a free parameter and the extinction curve of Calzetti et al. (2000) for starburst galaxies is adopted. The templates are broadened and shifted, up to  $1000 \text{ km s}^{-1}$  in velocity space, to match the observed spectrum. With the redshift noted above, we find that  $\Delta v = -40 \pm 30 \text{ km s}^{-1}$ . Emission line regions were masked during the fit. The best-fit starlight continuum is shown in Fig 1. The presence of Balmer absorption lines and lack of an apparent  $4000\text{\AA}$  suggest a recent/on-going starburst. An effective reddening of starlight is yielded to be  $E(B - V) = 0.65 \pm 0.05$  for the Calzetti *et al.*'s extinction curve, which is among the most dusty galaxies in the SDSS galaxy sample (Lu et al. 2006).

Considering the relative low S/N ratio of the HST-FOS spectrum, we fit the UV continuum with either a reddened simple stellar population (SSP) or a reddened power-law. Prominent emission lines are modeled with Gaussians in this fit with their widths and centroids as free parameters; these include C IV] $\lambda 1549$ , Si IV+O IV] $\lambda 1400$ , He II] $\lambda 1640$ , O III] $\lambda 1663$ , N III] $\lambda 1750$ , Al III] $\lambda 1860$ , N IV] $\lambda 1486$  Si III] $\lambda 1892$ , and C III] $\lambda 1909$ . Weak emission lines detected only marginally, such as Si II] $\lambda 1808, 1817$ , are not considered. The prominent emission line centered at  $\lambda 1782.4$  rest frame, which can be identified as blue shifted Fe II 191 (wavelength  $1787\text{\AA}$ ), is modeled with a Gaussian. In the worst case, wavelength zero point of FOS can be displaced up to  $250 \text{ km s}^{-1}$  (Keyes, HST Handbook), we will keep this in mind in the following analysis of the FOS data.

The SSP spectra  $f_{SB99}(\lambda)$  was taken from starburst99 models (Leitherer et al. 1999 ; Vázquez & Leitherer 2005 ). The high resolution SSP models are only available for the solar abundance with a wavelength coverage of  $1200 - 1870 \text{\AA}$ , and with ages from 1 to 20 Myr for either an instantaneous burst or a continuous star formation. To extend to the full wavelength range of the FOS spectrum, we use the interpolated low resolution model of Starburst99 for  $\lambda > 1870\text{\AA}$ . This is reasonable since the extrapolated wavelength range is rather small ( $\Delta\lambda = 50 \text{\AA}$ ) and free from strong stellar absorption lines. The UV continuum can be reasonably well fitted with this simple model (Fig 2). We use both SMC and Calzetti's extinction curves. But the best fitted model with Calzetti's extinction curve predicts an optical flux well above the SDSS spectrum, thus will not be discussed further. The best fitted model converges to a stellar population (1 Myr) and a moderate reddening  $E(B - V) \sim 0.26 \pm 0.03$  for the SMC extinction curve. The SFR rate is  $450 \pm 50 \text{ M}_{\odot} \text{ yr}^{-1}$  for instantaneous burst and  $430 \pm 40 \text{ M}_{\odot} \text{ yr}^{-1}$  for continuous formation models after scaled to a lower stellar mass cutoff of  $0.1 \text{ M}_{\odot}$ . For instantaneous model 2 Myr population yields significant worse fit ( $\Delta\chi^2 = 10$ ), however, for continuous formation model, 2 Myr population also yields reasonable fit ( $\Delta\chi^2 = 3$ ) with a factor of two smaller SFR  $230 \pm 20 \text{ M}_{\odot} \text{ yr}^{-1}$ . Note that only statistical uncertainty is quoted here, while much large errors may be introduced

by our assumptions, such as uniform dust reddening and ignoring intermediate age stellar populations. Thus the SFR value must be interpreted with care.

The optical spectrum, obtained by subtracting the best UV model, can be fitted with a reddened stellar population of an intermediate age around 0.90 Gyr (Fig 2), with a reddening of  $E(B-V) \approx 0.30$  using Calzetti et al.’s extinction curve. The derived stellar mass is  $9 \times 10^{10} M_{\odot}$ . Using the SMC extinction curve, we obtain a similar reddening ( $E(B-V) = 0.40$ ) and a slightly younger stellar population (0.64 Gyr) with a somewhat smaller total stellar mass (13% less). With those exercises, albeit with some uncertainties, we conclude that a few  $\sim 10^{10} M_{\odot}$  stellar mass has been built within the last Gyr in the host of Q 132+058. Note the older stellar population has a negligible contribution to the UV flux.

The power-law model yields a fit to UV spectrum as good as the SSP model. Therefore, we cannot distinguish two models from the UV fit alone. If both power-law index and reddening vary freely, they are poorly constrained. For an unreddened power-law, a slope of  $\beta = 2.0 \pm 0.2$  ( $f_{\lambda} \propto \lambda^{\beta}$ ) is obtained. Fixed the slope to typical quasar value  $\beta = -1.7$ , a reddening of  $E(B-V) = 0.28 \pm 0.02$  is yielded for SMC-type grain. However, extrapolating these models over-predicts severely the optical flux below 4000Å. Only when  $\beta \leq -6.0$ , the model flux is consistent with the optical flux with a large intrinsic reddening  $E(B-V) \geq 0.605$ . Not only such a flat UV spectrum has never been observed in quasars, but also the reddened corrected UV flux around 1400Å is a factor of 3600 times the observed value, which gives an UV luminosity well larger than the total infrared luminosity estimated in §4.2. Thus we believe that a single power-law model is not realistic.

## 2.2. Emission lines

We obtain the emission-line spectrum by subtracting the model continuum. The emission-line profiles are rather complex and show several distinct emission-line components (see Fig 3):

- C1** The low-ionization forbidden lines, [O II]  $\lambda\lambda 3726, 3729$ , [O I]  $\lambda 6302$ , [S II]  $\lambda\lambda 6717, 6732$  and [N II]  $\lambda 6584$  display a single-peaked profile at a redshift of  $z=0.20467$ , which can be taken as the systematic velocity. There is a corresponding peak in H $\beta$ , [O III]  $\lambda 5007$ . However, this component is absent in the ultraviolet lines.
- C4** The isolated UV lines C IV  $\lambda 1549$  and N III]  $\lambda 1750$  show a single-peaked profile, which can be well fitted with a Gaussian blueshifted by  $\sim 1,800 \text{ km s}^{-1}$  relative to the systematic redshift. This component is also evident in [Ne III]  $\lambda 3869$ , and [O III]  $\lambda 4959$  and in



[O III] $\lambda$ 5007, which is blended with the C3 of [O III] $\lambda$ 4959. The extended blue wing of Balmer lines, and C III], Si III] can be attributed to this component, too.

**C2** [Ne III] shows an additional component centered at the velocity around  $-500 \text{ km s}^{-1}$ . A peak at this velocity is also evident in [O III] $\lambda$ 5007, H $\beta$  line. It is likely the weak blue wing in the [O II] $\lambda$ 3727, [S II] and [O I] is due to this component, too. A comparison of H $\alpha$  line profile with those of low ionization lines such as [S II], [O II], [O I] and [N II] also suggests such a component in H $\alpha$ .

**C3** Both C III], H $\beta$  and [O III] show extended red wing up to a velocity of  $\sim 1,500 \text{ km s}^{-1}$ , which is not present in [O II], [S II], C IV and N III. Note that the redside of [Ne III] $\lambda$ 3869 is affected by both He I and [Fe VII] $\lambda$ 3890, thus it is not clear if this component is also present in [Ne III].

C1 and C4 are well defined from the isolated lines such as C IV, N III], [S II], [O I], and [O II]. One gaussian can adequately describe these components. C2 and C3 are less cleanly defined due to their blending with other components. It is interesting to note that the velocity separation between C1 and C2 is very close to the separation ( $490 \text{ km s}^{-1}$ ) of two peaks detected in the OH maser profile (Darling & Giovanelli 2002). In the following fit, we will use a gaussian for all components. The good fit to the C III]+Si III] blending with only C3 and C4 components indicates that C3 can be approximately described with a gaussian. While a gaussian C2 component yields also reasonable fit to the optical lines suggests that such approximation is acceptable.

Note in passing, the prominent emission line at  $1782.4 \pm 0.2 \text{ \AA}$  has a width of  $\sigma = 387 \pm 34 \text{ km s}^{-1}$  and flux of  $(189 \pm 14) \times 10^{-17} \text{ erg cm}^{-2} \text{ s}^{-1}$  (see also the lower panel in Figure 2). The line width is significantly broader than those of C1 and C2, but much narrower than those of C3 and C4. The line can be identified as blended of Fe II multiplet 191 ( $1785.26, 1786.74$  and  $1788.07 \text{ \AA}$  with intensity ratios 20:20:18). After taking into account of different instrumental resolution and line blending, the line center and width are consistent with the C2 component.

In order to obtain more physically meaningful fit, we tied the center and width of each component to be same for different lines. The flux ratio of multiplets is either fixed at its theoretical value or set as a free parameter. The [O III] $\lambda$ 4959/ $\lambda$ 5007 is fixed at its theoretical value of 1/3 for C1, C2 and C3, and is allowed to vary for C4. N III] $\lambda$ 750 consists of a blend of five lines at  $1746.82, 1748.65, 1749.67, 1752.16$  and  $1754.00 \text{ \AA}$ , and their relative ratios are fairly constant at density below  $10^{7.5} \text{ cm}^{-3}$ . We fixed the branch ratios at 0.03, 0.096, 0.502, 0.355, 0.097 as predicted by CLOUDY (See Appendix 1). C IV has two multiplets with a separation of  $500 \text{ km s}^{-1}$ . The multiplet ratio ( $1548/1551 \text{ \AA}$ ) is constrained in the range 2.0

to 1.0. We assume that  $\lambda 1900$  blending features are dominated by Si III] and C III], rather than by their forbidden counterparts. Justification for these assumptions can be found in Appendix 1. To couple with the systematic wavelength calibration uncertainty of FOS, which can be up to on diode (or  $250 \text{ km s}^{-1}$ ), we allow all UV lines to be systematically shifted up to  $250 \text{ km s}^{-1}$ . We assume that each line in the [N II] and [S II] doublets has the same profile. The [N II] $\lambda 6583/\lambda 6548$  ratio is set to its theoretical value of 3/1. The O III] $\lambda 1660/\lambda 1666$  doublet ratio is fixed to 1/2.4 for C3 and C4. The initial values for the centroid and width of each component are estimated by fitting individual lines with a Gaussian: [S II], [O I], [O II], and [N II] for C1; [Ne III], [O III] and H $\beta$  for C2 and C3; and C IV, N III], and [O III] for C4. A total of 19 emission lines are fitted simultaneously, including C IV, N III], Al III, Si III], C III], [O II], [Ne III], H $\gamma$ + [O III] $\lambda 4363$ , H $\beta$ , [O III] $\lambda\lambda 4959, 5007$ , [O I] $\lambda 6302$ , H $\alpha$ + [N II] $\lambda\lambda 6548, 6584$ , [S II] $\lambda\lambda 6717, 6731$ , He II $\lambda 1640$ , O III] $\lambda\lambda 1660, 1666$ , N IV $\lambda 1486$  and FeII 191. The final fit is shown in Fig. 3.

Balmer decrements are very different for different components from above decomposition: C2 has the largest H $\alpha$ /H $\beta$  ratio of 12, following by C1 (6.2), C3 (5.1) and C4 (4.2). Both of them are considerably steeper than 3.1 for an unreddened AGN. If this is interpreted as due to dust reddening, then C2 is heavily obscured while the others are mildly extinguished. In order to see if this is caused by the decomposition procedure, we plot H $\alpha$ /H $\beta$  at different velocity bin. Here, H $\alpha$  profile is obtained by subtracting the best-fit [N II] model from the observed spectrum. Because C1 is well defined and C2 is weak for [N II], [N II] subtraction should not introduce substantial uncertainty. The result is shown in Fig 5, where the data are adaptively rebinned to ensure the S/N ratio in each bin. Obviously, the Balmer decrement varies dramatically across the profile: it rises slowly from  $-4000$  to  $-1000 \text{ km s}^{-1}$ ; then increases sharply from  $-800 \text{ km s}^{-1}$  and reaches its maximum of  $H\alpha/H\beta \sim 10$  at the C2 centroid and then decreases rapidly to the red wing. Thus large Balmer decrement of C2 is independent of the detailed line decomposition. The well defined profile of Balmer decrement provides an additional evidence for C2 as a distinct component.

### 3. Physical Interpretation of Emission Line Components

We have decomposed empirically the emission lines into four components. In this section, we will try to give a physical interpretation for those components based on the physical conditions that are required to reproduce the observed emission line ratios. We will use the photoionization models as a guideline in the following discussion, but keep in mind that shocks may also play certain roles giving the presence of outflows indicated by blue-shifted line profiles.



### 3.1. Component 1

C1 has doublet ratios of  $[\text{S II}]\lambda 6716/[\text{S II}]\lambda 6731 \simeq 1.5$  and  $[\text{O II}]\lambda 3729/[\text{O II}]\lambda 3726 \simeq 0.70$ , which reach their low density limits, and hence the density of the emitting gas should be no larger than a few hundred  $\text{cm}^{-3}$ . However, its classification is ambiguous on the conventional BPT diagram (Baldwin et al. 1981; Kewley et al. 2006). On the  $[\text{N II}]/\text{H}\alpha$  versus  $[\text{O III}]/\text{H}\beta$  diagram (Fig 4), C1 is very close to the extreme H II curve of Kewley et al. (2001). It is in the regime for LINER on  $[\text{O I}]\lambda 6303/\text{H}\alpha$  vs  $[\text{O III}]/\text{H}\beta$  diagram, but on the H II side on the  $[\text{S II}]/\text{H}\alpha$  vs  $[\text{O III}]/\text{H}\beta$  diagram. The Balmer decrement  $H\alpha/H\beta \approx 6.1 \pm 1.6$  indicates substantial reddening ( $E(B - V) = 0.61 \pm 0.26$  mag, assuming an intrinsic  $H\alpha/H\beta = 3.0$ ). With such a reddening, the weakness of the corresponding component in the UV lines can be explained naturally. With an observed ratio  $[\text{O II}]\lambda 3727/[\text{O III}]\lambda 5007 \simeq 7.3$ , the reddening-corrected ratio would be around 14, extreme among the LINERs (Kewley et al. 2006). This puts it on the border between H II and LINER on the  $[\text{O I}]/\text{H}\alpha$  vs  $[\text{O II}]/[\text{O III}]$  diagram. This component can be a mixture contribution from H II and AGN, a combination of photoionization and shock-excitation, or gas ionized by a diluted AGN continuum (Dopita & Sutherland 1996).

### 3.2. Component 2

At first glance, C2 is formed in the star forming regions.  $[\text{N II}]$ ,  $[\text{S II}]$ , and  $[\text{O I}]$  emission lines is relatively weak with respect to  $\text{H}\alpha$ . Those line ratios fall well in the H II locus on all three BPT diagrams (Fig 4). The gas has a relative low metallicity ( $Z \sim 0.2 - 0.3 Z_{\odot}$ ), according to  $[\text{N II}]/\text{H}\alpha$  ratio (Pettini & Pagel 2004; 6). However, giving the high luminosity of the galaxy, the low gas metallicity is not expected. In addition, large  $[\text{Ne III}]\lambda 3869/[\text{O III}]\lambda 5007 \simeq 1.15$  requires a rather high gas density ( $> 10^7 \text{ cm}^{-3}$ ). Even higher density is required if the large Balmer decrement of C2 is attributed to dust reddening. In this case, weakness in  $[\text{N II}]$ ,  $[\text{S II}]$  and  $[\text{O I}]$  is naturally explained because they are collisionally de-excited, and BPT diagrams no long provide diagnostics for the ionizing source, as such the ionizing source can be AGN as well.

The strong Fe II 191 emission in component 2 is a puzzle. First, its emission region cannot be reddened as severely as indicated by the apparent Balmer decrement, which suggests an intrinsic dust reddening of  $E(B-V)=1.2$  mag using Calzetti’s extinction curve for an intrinsic  $H\alpha/H\beta=3.0$ . This indicates either a large intrinsic  $H\alpha/H\beta$  or a separated Fe II 191 emission region. Second, because of lack a similar component in other UV lines, Fe II 191 must be produced in a region shielded from intensive Uv ionizing radiation. While whether this can be consistent with the prominent emission in  $[\text{O III}]$  and  $[\text{Ne III}]$  needs to be further

studied, a large column density may explain this. Third, Fe II 191 is strong while optical Fe II emission is weak. The dominance of emission from high excitation levels indicates that either it is formed in a high temperature and dense HI region or/and through UV photon excitation by the continuum radiation (PCR). A high temperature and dense HI region may help to explain  $H\alpha/H\beta$  ratio in this component through collisional enhancement of  $H\alpha$  emission. Because this component is blueshifted by  $350 \text{ km s}^{-1}$  with respect to the systematic velocity, interaction between the outflow and interstellar medium may be a viable heating source. PCR process had been suggested for the Fe II emission from the wind of spectroscopic binary KQ Puppis (Redfors & Johansson 2000). In order to make photon-pumping effective, the gas must see a strong soft UV photons and has large internal velocity gradient. We speculate that an ionizing continuum filtered by a thin partial ionized source may mimic the soft UV photons (see a similar idea in Collins et al. 2009). The PCR process would also produce Fe II 193 emission lines at 1459, 1465, 1474Å but the spectrum quality does not allow us to assess their existence.

Therefore, we tentatively interpret this component as from a dense region : The large Balmer decrement is interpreted as due to radiation transfer effect or caused by collisional excitation in the warm dense HI region, rather than dust reddening; Fe II 191 is produced either in a high temperature warm HI region or through PCR process; [N II], [S II] are suppressed by collisional de-excitation. The blueshift of C2 ( $350 \text{ km s}^{-1}$ ) relative to the systematic velocity can be readily interpreted as from an outflow with the far-side, redshifted counter-flow being obscured. However, we cannot rule out the possibility that C2 consists of emission lines from a dusty star forming region and an additional dense warm partially ionized gas component.

### 3.3. Component 3

C3 has strong Si III], C III], Al III, [O III], [Ne III] and Balmer lines, but is undetected or very weak in C IV, N III], [O I], [O II], [S II] and [N II]. Relatively high ionization and excitation suggest that this component is produced by AGN photoionization.  $O \text{ III}]1665/[O \text{ III}]5007$ ,  $C \text{ III}]1909/[O \text{ III}]5007$  and  $[O \text{ III}]5007/H\beta$  suggest a density of  $10^{7.5-8} \text{ cm}^{-3}$ , while  $[O \text{ III}]\lambda 4363/\lambda 5007$  and  $[Ne \text{ III}]3896/[O \text{ III}]5007$  indicate a somewhat lower gas density about  $10^7 \text{ cm}^{-3}$ . As  $[O \text{ III}]\lambda 4363$  is badly blending with  $H\gamma$  line and the flux of [Ne III] is sensitive to the way of modeling the red wing, the latter two should be used with care. Therefore, we believe that  $10^8 \text{ cm}^{-3}$  is more likely the real value.

However, the large line ratio of  $Si \text{ III}]/C \text{ III}] \sim 1$  can only be reproduced with a high density  $n_H > 10^{9.5} \text{ cm}^{-3}$ , if the gas has abundances being the solar or the scaled solar values

(See Appendix 2). This may be explained in terms of at least two emission line regions with different densities. Such models, however, have certain drawbacks as the following. If the high and low density gases are at the same distances and see the same continuum, the large difference in density would result in an ionization parameter for the low density gas being three orders of magnitude higher than that for the high density gas; this would lead to strong coronal emission lines, such as [Fe VII], which are not seen in the observed spectrum.

A single zone model can be constructed if Si element is enhanced relative to C. Overabundance of  $\alpha$ -elements relative to C is predicted by the starburst chemical evolution models for quasar host galaxies (Haimann & Ferland 1993). Considering the fact that Q1321+058 experienced a recent starburst (see next section), this chemical enrichment route is plausible. In their models, more massive stars are produced with respect to star formation in the Galaxy, thus leads to both fast metal enrichment and a high final metal abundance ( $\geq 10 Z_{\odot}$ ).  $\alpha$ -elements are enhanced relative to C because C-enrichment from intermediate mass stars has a finite time delay with respect to SN II+Ib eruption, which produces most  $\alpha$ -elements. It should be noted that the relative abundances of different metals depend on the metallicity. With increasing metallicity, N relative to O increases very fast at all abundances, while Fe and  $\alpha$ -elements rise substantially. Lack of N III], N IV] and C IV], we can only put an upper limit on the gas metallicity to 3 solar value based on N III]/C III] because other lines are not sensitive to the metallicity.

Over the density range considered in Appendix 2, Si III]/C III] provides a good diagnostics of the ionization parameter. The observed Si III]/C III] ratio can be reproduced with two branches of ionization parameters: an upper branch with  $\log U \sim -0.5$  and a lower branch  $-2.0 \leq \log U < -1.5$ , at a column density  $\log N_H(\text{cm}^{-2}) = 21$ . At larger column densities, we find that only the low ionization branch is possible, however. In the density range, C III]/C IV] is sensitive both to the ionization parameter and to the column density. The lower limit on C III]/C IV] suggests a large column density  $\log N_H \geq 22$  and a low ionization parameter  $\log U < -2.2$ , thus the lower branch solution is preferred. With  $n_H \sim 10^{7.5} \text{ cm}^{-3}$ ,  $\log U \sim -2.0$  and  $\log N_H \geq 22$ , the observed line ratios can be reproduced roughly. The relatively high density can also explain naturally the weakness of this component in [O II], [N II], and [S II].

With a relative large emission line width and close to systematic velocity, this component may be gravitational bound optical thick clouds ionized by the AGN continuum. We speculate that it is the intermediate emission line region between BLR and NLR.

### 3.4. Component 4

C4 is present in all permitted and semi-forbidden lines, as well as the high-ionization forbidden lines [O III] and [Ne III]. The line ratios [O III]4363/[O III]5007, [O III]1665/[O III]5007, [C III]1909/[O III]5007, and  $H\beta$ /[O III]5007 give consistent densities around  $10^7 \text{ cm}^{-3}$ , while [Ne III]3869/[O III]5007 suggests a somewhat lower density ( $10^{6.6} \text{ cm}^{-3}$ ). These line ratios are only weakly dependent on the metal abundances or gas column density, thus we believe the density is quite robust. As for C3, at this density range, a large [Si III]/[C III] requires that Si is over-abundant relative to C, and this may be interpreted as the starburst abundances of Haimann & Ferland (1997). Large [N III]/[C III] ratio can be reproduced only with a very supersolar abundance ( $Z \sim 10Z_{\odot}$ ; see Fig 7) because nitrogen abundance increases with the average metallicity ( $Z$ ) as  $\propto Z^2$  at high  $Z$  in their models.

As seen in Fig 7, we are unable to reproduce quantitatively all line ratios with a single constant density models described in Appendix B, but we believe this can be solved by adjusting the input ionizing continuum. Metallicity independent line ratios, [C III]/[C IV] and [N III]1750/[N IV]1846 suggests different ionization parameters  $\log U \simeq -1.5$ , and  $\log U \simeq -2.5$  for a range of gas column densities. Since the ionization potential of  $N^{2+}$  ( $N^+$ ) is only slightly larger than  $C^{2+}$  ( $C^+$ ), any smooth change in the continuum slope in this regime is not likely to cause such big difference. However, we note that the ionization potential (55.45eV) of  $N^{2+}$  is just above that of He II ionization potential, while that (47.89eV) of  $C^{2+}$  is below the He II ionization potential. If the continuum incident on the gas has already been filtered by a relative highly ionized gas that is optically thick to helium ionizing photons, such ionizing continuum will have less  $N^{2+}$  ionizing photons relative to  $C^{2+}$  ionizing photons, resulting more less  $N^{3+}$  ions. It would be interesting to see if such a model can reproduce [N III]/[N IV] and [C III]/[C IV] ratio at the same time, but throughout photo-ionization calculations are beyond the scope of this paper. We only want to point out here that once such an ionizing continuum is adopted, the ionization parameter will be close to, but substantially larger than, the higher ionization parameter estimate based on [C III]/[C IV] ratio. Therefore, we interpret C4 as a dense outflow driven by AGN.

## 4. Discussion

### 4.1. Outflows

In Q 1321+058, we have detected emission lines from two outflow components, C2 and C4. The broad component C4 with a radial velocity  $1650 \text{ km s}^{-1}$  has been interpreted as dense, metal enriched outflow photoionized by AGN continuum, probably filtered by an

ionized absorber in last section. The narrow component C2 is also produced by dense gas, but its nature is less clear. Therefore, we will focus on the mass outflow rate and kinematic power of the high velocity outflow C4 in this section first, and then discuss briefly the C2 component.

We first estimate the mass in the outflow for C4. The H II mass of the outflow can be estimated from the H $\alpha$  luminosity as follows

$$M = \frac{1.4m_H L_{H\alpha}}{n_e \alpha_{H\alpha}^{eff} h \nu_{H\alpha}} = 450 \times \left( \frac{L_{H\alpha}}{10^{42} \text{erg s}^{-1}} \right) \left( \frac{n_e}{10^7 \text{cm}^{-3}} \right)^{-1} M_{\odot} \quad (2)$$

assuming case-B recombination with a temperature of  $10^4$  K (Table 4.2 of Osterbrock 1989). The factor 1.4 accounts for Helium mass. With the H $\alpha$  luminosity of  $1.5 \times 10^{42} \text{ erg s}^{-1}$ , we obtain  $\sim 680(n_e/10^7)^{-1} M_{\odot}$  for the high velocity outflow. This mass should be regarded as lower limits to the total mass in consideration of the existence of possible HI regions. We can estimate the mass of emission line gas using the best model in section 3 as well. The model gives a similar value  $\sim 400 M_{\odot}$ .

For the single zone photoionization models discussed in §3.1, we estimate the distance of the outflow to the AGN,

$$R = \sqrt{\frac{Q_{ion}}{4\pi n_H U c}} = 150 \sqrt{\frac{10^7 \text{ cm}^{-3}}{n_H} \frac{0.01}{U}} \text{pc}. \quad (3)$$

Assuming a typical quasar SED (Richards et al. 2006), the total ionizing flux of Q 1321+058 is estimated to be  $8 \times 10^{57} \text{ photons s}^{-1}$  (see §4.2). Using the density and ionization parameter estimated in §3.1, we find distances of  $\sim 80 \text{ pc}$  for C4, which is one order of magnitude smaller than the size of NLR in quasars of similar bolometric luminosity (Benert et al. 2005). Note the distance is not very sensitive to the ionization parameter used.

The mass loss rate is small compared to the mass accretion rate onto the supermassive black hole. The emission line gas is visible for a dynamic time scale of  $\Delta R/v_r$ , where  $\Delta R$  is the visible radial length of the outflow, and  $v_r$  is the observed radial velocity. By combining with the mass in Eq 2, we obtain an estimate of the mass loss rate,

$$\dot{M} = \frac{M v_r}{\Delta R} = 2 \times 10^{-2} \left( \frac{L_{H\alpha}}{10^{42} \text{erg s}^{-1}} \right) \left( \frac{10^7 \text{ cm}^{-3}}{n_e} \right) \left( \frac{v_r}{2000 \text{ km s}^{-1}} \right) \left( \frac{100 \text{ pc}}{\Delta R} \right) M_{\odot} \text{ yr}^{-1} \quad (4)$$

Note with the column density estimated in the section §3, the corrections due to HI gas are within a factor of two. The mass loss rate is order of  $0.03 M_{\odot} \text{ yr}^{-1}$  if  $\Delta R/R \sim 1$ . Therefore, the mass loss rate for these outflow is not important with respect to the mass accretion rate onto the supermassive black hole (see next section).

The C4 outflow does not provide sufficient kinetic power to account for the feedback that is supposed to heat the cold gas in the host galaxy up to the escape velocity. The kinetic power with the line emitting gas is only on the order of  $\sim 10^{-6}(100pc/\Delta R) M_{\odot}c^2 \text{ yr}^{-1}$ , or  $10^{-5}(100pc/\Delta R)$  of the AGN bolometric luminosity according to the mass loss rate in Eq 4 and the observed outflow velocity, while a few percent is required for the flow to be energetically important (e.g., Di Matteo et al. 2005). A similar conclusion has been reached by modelling absorption lines for nearby Seyfert galaxies (Crenshaw, Kraemer & George 2003).

However, instead to conclude that outflows are energetically un-important for AGN-galaxy feedback, we argue below that there is an indication for much larger kinetic power than the above estimate. As we have seen in the last section that the column density of the emission gas is fairly low, of order of  $10^{21} \text{ cm}^{-2}$ . A gas cloud with such column density, density and typical temperature of photoionized gas is not bounded by self-gravity, thus it will either disperse away on the time scales of only 10 years (i.e.,  $\Delta R \sim 2 \times 10^{-2} \text{ pc}$ ) or be confined by external pressure. In the former case, continuous formation of the line emitting gas is required, and the mass outflow rate would be  $40 M_{\odot} \text{ yr}^{-1}$ , and total kinetic power would be three magnitude higher than the above estimate, which is sufficient to explain AGN-galaxy feedback. In the latter case, the confined medium can be hot phase gas. Since the filling factor of the warm gas is extremely small ( $\sim 10^{-10} \times \frac{100 \text{ pc}}{\Delta R}$ ), the bulk of the gas will be in the hot phase, and both the mass loss rate and the kinetic power may be much larger than above estimate. Hot gas has been detected in nearby ultra-luminous infrared AGN including NGC 6240 (Komossa et al. 2003). Future high spatial resolution X-ray observations can be used to examine if such a hot X-ray component presents in this quasar as well.

The covering factor of the emission line regions can be estimated from the ratio of  $\text{H}\alpha$  to the ionizing photon flux assuming Case-B recombination if the emission line region is optically thick to the ionizing photons. It turns out that the covering factor of C4 is as small as  $6 \times 10^{-5}$ . Similar numbers (order of  $\sim 10^{-4}$ ) are also obtained by comparing the  $\text{C III}]1909$ ,  $[\text{O III}]\lambda 5007$  or  $\text{H}\alpha$  luminosity with the best photoionization model in the last section in combination with above distances. For comparison, the covering factor of the NLR in quasars is typically a few percent according to simple photon-counting estimation (e.g., Netzer & Laor 1993). Thus, the AGN outflows in Q 1321+058 has a covering factor 100 times smaller than a typical NLR.

In passing, with a maximum velocity extending to  $\sim 4000 \text{ km s}^{-1}$  and emission lines of a wide ionization range, Q1321+058 would appear as a LoBAL quasar if the line of sight to the nuclear continuum is intercepted by the outflow. We speculate that Q 1321+058 is an



obscured, high luminosity version of MKN 231, an extensively studied infrared luminous low ionization BAL QSO with an extended outflow region on kpc scale (e.g. Lípari et al. 2005 ). The requirement of a soft ionizing continuum for C4 is also consistent with weak X-ray emission from BAL QSOs.

We would like to point out that the properties of outflow in C2 component is very uncertain. First, Fe II emission requires an extensive warm HI region, but its column density cannot be properly constrained without extensive modelling of the FeII emission. Thus, Eq (4) will give only a lower limit to the mass loss rate. Second, if a large fraction of  $H\alpha$  photons are produced through collision excitation as is required to explain its large intrinsic Balmer decrement, Eq (4), on the other side, Eq (4) is no long valid. Finally, it has yet to be demonstrated that collisional excitation can fully explain the large  $H\alpha/H\beta$ . Otherwise, dust extinction may be important.

## 4.2. Quasar Activity and Star Formation History

The broad band spectral energy distribution (SED) of Q 1321+058 is plotted in Fig. 6. The near-infrared data are taken from the two micron all sky survey (2MASS Skrutskie et al. 2006). The mid- and far-infrared data are drawn from observations by the infrared space observatory (ISO) (Kuraszkiewicz et al. 2003 ) and the IRAS faint source catalog (Moshir et al. 1990 ), respectively. Q1321+058 was also observed with Spitzer IRAC and IRS instruments (Farrah et al. 2007; Sirocky et al. 2008). The SDSS and HST FOS spectra, as well as the SDSS photometric data corrected for Galactic extinction are also plotted.

The mid-infrared bump is very prominent in the SED, that rises steeply from near- to mid-infrared, and then flattens and declines in far-infrared. There is no apparent dip or peak around 9.7 micron in the source rest frame. Lack of strong emission or absorption feature is confirmed by Spitzer IRS observation, which reveals only weak silicate absorption feature(9). The flat middle to far-infrared spectrum and a lack of prominent PAH features suggest that the bulk of the mid-infrared emission is powered by the hidden quasar (Weedman et al. 2005 ; Hao et al. 2007). To compare the observed SED with that of red quasars, we redden the average SED of infrared luminous quasar from Richards et al. (2006) through a uniform dust screen with  $E(B - V)=4.5$  using the extinction curve of Weingartner & Draine (2001; 30ppm C in PAH), which can reproduce approximately the extinction curve to the Galactic center. The result is also shown in Fig. 3. This over-simplified model can reproduce the overall shape of the infrared SED except for predicting a strong dip around 10  $\mu\text{m}$  due to small grains (see also Laor & Draine 1993 ), which can be eliminated with a detail treatment of radiative transfer (e.g. Siebenmorgen et al. 2004 ).

The  $12\mu\text{m}$  to total observed [O III] flux ratio is 50 time higher than the average Seyfert galaxies (Haas et al. 2007). Even after correcting for reddening, this ratio is still more than a factor of ten higher. However, we consider that this can be attributed to weak [O III] emission rather than the dominance of mid-infrared flux from the star-formation region for the aforementioned reason. Note weak [O III] emission is a common characteristics of low ionization BAL QSOs (Boroson & Meyers 1993).

The total luminosity in the infrared is  $1.9 \times 10^{46} \text{ ergs s}^{-1}$ , which makes Q 1321+058 an ULIR quasar. If Q 1321+058 bears an intrinsic SED of a typical quasar, the bolometric luminosity is estimated to be  $3.9 \times 10^{46} \text{ ergs s}^{-1}$ , using the quasar template fit to infrared SED and integrating in the optical to UV portion <sup>2</sup>. However, if the covering factor of dust in this object is larger than the average value of quasars, the bolometric luminosity is then over-estimated from the above fit. A conservative estimate can be given by assuming that all of the UV to X-ray continuum emission is absorbed and re-emitted isotropically in the infrared. This yields a bolometric luminosity a factor of two smaller. The mass accretion rate is thus  $\sim 3\text{-}6 M_{\odot} \text{ yr}^{-1}$ , for the typical radiative efficiency of 0.1. If the quasar is accreting at close to the Eddington limit, the black hole mass is estimated to be around  $10^8 M_{\odot}$ .

The SFR for this object may be estimated in several ways. We have found that UV spectrum can be fitted by a young stellar population. With the age and mass of the young stellar population, we estimate a SFR of about  $450\text{-}230 M_{\odot} \text{ yr}^{-1}$ . However, as we noted this number is only valid to the order of magnitude giving our oversimplified assumption about the model. Alternatively, using the UV continuum luminosity, the SFR calibrator of Madau et al. (1998) and assuming an extinction  $E(B-V)=0.26$ , we obtain a SFR of only  $45 M_{\odot} \text{ yr}^{-1}$ . The discrepancy arises because the SSP model contains 1 Myr population only, while older stellar populations still contribute to the observed UV flux. The SFR can also be estimated from the far-infrared luminosity and radio power. Assuming most of the far-infrared luminosity is powered by the starburst (e.g., Schweitzer et al. 2006), we find an upper limit to SFR of about  $270 M_{\odot} \text{ yr}^{-1}$ , similar to that seen in NGC 6240 (e.g., Pasquali, Gallagher & de Grijs 2004). Q 1321+058 was detected in both NVSS and FIRST with a flux density of  $S_{1.4\text{GHz},\text{NVSS}} = 4.9 \pm 0.5 \text{ mJy}$  and  $S_{1.4\text{GHz},\text{FIRST}} = 4.5 \pm 0.3 \text{ mJy}$ . Assuming that the radio emission ( $6 \times 10^{30} \text{ erg s}^{-1} \text{ Hz}^{-1}$ ) all comes from the H II region, we obtain an upper limit of  $SFR \lesssim 330 M_{\odot} \text{ yr}^{-1}$ . These values are consistent with that derived from the UV spectral fit. The SFR can be also estimated with the PAH luminosity (10, e.g.). (author?) (Cao et al. 2008) detected a  $6.2\mu\text{m}$  PAH luminosity of  $1.2 \times 10^{42} \text{ erg s}^{-1}$ . Following Hernan-Caballero et al. (2009), we obtain a SFR of only  $4.6 M_{\odot} \text{ yr}^{-1}$ . Finally, the

---

<sup>2</sup>Infrared emission is the dust reprocessed light from the optical and ultraviolet continuum, thus should not be counted in the bolometric luminosity calculation for an unobscured quasar.

SFR can be estimated from  $H\alpha$  luminosity. An upper limit can be derived if C1 is assumed to be ionized by young stars. The extinction corrected  $H\alpha$  luminosity for C1 are  $1.8 \times 10^{42}$  erg s $^{-1}$ . According to the calibration of Madau et al. (1998), the SFR is  $14 M_{\odot} \text{ yr}^{-1}$ . SFR will be one order of magnitude larger if C2 is from star-formation region. The very different SFR derived from different methods demonstrate the difficulty of estimating SFR in the presence of AGN activity.

With all above estimates, SFR does not likely exceed hundreds  $M_{\odot} \text{ yr}^{-1}$ , while we have found a mass accretion rate of  $3\text{-}6 M_{\odot} \text{ yr}^{-1}$  to the black hole according to its bolometric luminosity. The  $\dot{M}/SFR$  is more than an order of magnitude larger than that required for the strict co-evolution of the black hole and bulge. However, the black hole to stellar mass ratio can still be consistent with that found in local spheroidal galaxies (Gebhardt et al. 2000). The mass of the intermediate-aged stellar population in Q 1321+058 is  $\sim 6 \times 10^{10} M_{\odot}$  from our analysis of the SDSS and HST spectra. If the bolometric luminosity does not exceed the Eddington luminosity, a lower limit to the black hole can be set to  $10^8 M_{\odot}$ . It was argued that ultraluminous infrared quasars are accreted at the Eddington limit rather than fuel limited (Hao et al. 2005). Then a lower-limit on a mass ratio of the black hole to the intermediate and young stellar populations to be  $\sim 2 \times 10^{-3}$ , in coincidence with that for local spheroidal galaxies (Gebhardt et al. 2000).

## 5. Summary

We have performed a detailed analysis of the optical–UV spectrum and the broad band spectral energy distribution of Q 1321+058. Our analysis confirms that it is an obscured quasar with its bulk energy output in mid-infrared. Its optical–UV spectra show complex emission lines. We identified four components: a narrow component at the systematic velocity (C1), a narrow component at velocity  $-380 \text{ km s}^{-1}$  (C2), and two broad components at  $-80 \text{ km s}^{-1}$  (C3) and  $1650 \text{ km s}^{-1}$  (C4), respectively. C1 shows a LINER/composite spectrum, which is common among ULIRGs. Both C2 and C4 can be interpreted as dense outflows with the back-sides are obscured. We speculate that C3 comes from an intermediate line region between BLR and NLR.

A comparison of the measured emission line ratios with photo-ionization models suggests that C4 outflow has a gas density  $n_H \sim 10^7 \text{ cm}^{-3}$ , column density  $N_H \sim 10^{21} \text{ cm}^{-2}$ , an  $\alpha$ -enriched super-solar metallicity of  $Z \sim 10 Z_{\odot}$  for starburst galaxies. It is located at a distance about a hundred parsecs from the central continuum source. The velocity range, ionization level, and column density derived from the emission lines suggest that Q 1321+058 might be a low ionization broad absorption line (LoBAL) quasar viewed in an “unfavored”

direction, with the outflows being part of the otherwise LoBAL region. The apparent total mass loss rate in the C4 outflow is small, thus the outflow associated with line emitting gas does not have sufficient energy to remove the ISM of host galaxies, quenching both star-formation and accretion process. But we argued that the optical emission line region may trace only a small amount of quasar outflows, thus the actual mass loss rate and kinetic power may be much larger. The covering factor of the outflow is very small.

The optical and UV continuum can be well modeled with a young ( $\sim 1 \text{ Myr}$ ) plus an intermediate age ( $0.5 - 1 \text{ Gyr}$ ) stellar population. The latter population has a mass around a few  $10^{10} \text{ M}_{\odot}$ , suggesting for a recent building of a massive galaxy following the merger of two gas rich galaxies. Fast stellar mass building is also consistent with the metallicity that required to explain the C3 and C4 line ratios. We obtain very different SFR or its upper limits, independently from UV continuum, radio, far-infrared and emission line luminosity in the range of a few to several hundred  $\text{M}_{\odot} \text{ yr}^{-1}$ . We estimate a bolometric luminosity of  $(2-4) 10^{46} \text{ erg s}^{-1}$  for the quasar, or a mass accretion rate of  $3-6 \text{ M}_{\odot} \text{ yr}^{-1}$  for a typical efficiency of 0.1. The SFR to mass accretion ratio is more than one order of magnitude lower than that is required for the co-evolution of black hole and spheroid. If the black hole is accreted at the Eddington rate, the black mass to the stellar mass ratio will be coincident with that defined by local spheroid galaxies.

We thank the anonymous referee for constructive comments which lead to significant improvement in the presentation. This work is supported by Chinese Natural Science Foundation through CNSF-10233030 and CNSF-10573015, and by the Knowledge Innovation Program of the Chinese Academy of Sciences, Grant No. KJCX2-YW-T05. H. Y. Zhou acknowledges the Chinese NSF support through NSFC-10473013, and the support from NSF AST-0451407 and AST-0451408, NASA NNG05G321G and NNG05GR41G, and the University of Florida.

#### A. Notes on the fit to [O III], N III] and Si III] emission lines

Initially, we fit the four components to the [O III] $\lambda\lambda 4959, 5007$  blend, and for each component the doublet ratio is fixed to 1/3. The fit is not satisfactory. In particular, there is an excess in the blue component in [O III] $\lambda 4959$ . This indicates that the doublet ratio of one or more components is not the theoretical value, or there is contribution from other emission line(s). Potential contaminating lines in the regime can be [Fe VII] $\lambda 4989$ , He I $\lambda 5016$ , [Fe III] $\lambda\lambda 4988, 4931$  or the Fe II blend. Since the Fe II bumps around  $4700 \text{ \AA}$  and

5100 Å is not visible, we will not consider this as a likely possibility<sup>3</sup>. Our grid photo-ionization calculation suggests that the He I emission should be no more than 2% of H $\beta$  in strength (for a wide range of parameters as discussed in Appendix 2), and is too weak to account for the excess. [Fe VII]  $\lambda$ 4989 can be fairly strong for a high ionization parameter and a low column density in photoionization models, but [Fe VII]  $\lambda$ 6087, which is not detected in our spectrum, should be a factor of at least 2.7 stronger for all models. Therefore, it is likely that the excess is due to the [O III]  $\lambda$ 4959 emission. To incorporate this, we leave the [O III]  $\lambda$ 4959/ $\lambda$ 5007 ratio of the blue component as a free parameter. This gives fairly good fit with the ratio of 0.46. Therefore, in the subsequent fit, the [O III] doublet ratio is allowed to vary freely for C4 and is fixed at 1/3 for other components.

The N III]  $\lambda$ 1750 emission is a blend of five lines, and the multiplets ratios depend on both gas temperature and density (Dwivedi et al. 1995 ). Using the grid photo-ionization models described in Appendix 2, we estimate that this feature is dominated by N III]  $\lambda$ 1751 and N III]  $\lambda$ 1752, and other lines of the multiplets account for less than 10% only. The line ratios are only weakly depends on the ionization parameters, we fixed the multiple ratios at the model value in the vicinity of the best model density.

Both Si III]  $\lambda$ 1889 and [Si III]  $\lambda$ 1883 may contribute to the  $\lambda$ 1888 blend. At a low density, [Si III] is the main contributor to this feature, while at a density above  $10^6 \text{ cm}^{-3}$  this feature is dominated by Si III]. The situation is similar for the  $\lambda$ 1909 blend of [C III]  $\lambda$ 1907 and C III]  $\lambda$ 1909. As aforementioned, the Si III]/C III] ratio requires this feature being dominated by semi-forbidden transitions. Therefore, we take wavelengths 1889Å and 1909Å for Si III and C III, respectively, in the following analysis.

## B. Photoionization Models

We have computed large grid constant-density models using the photoionization code CLOUDY (version 06.02, last described by Ferland et al. 1998). The range of gas density considered is  $10^{2-10} \text{ cm}^{-3}$ , and the range of ionization parameter considered is  $-3.5 < \log U < 0.0$ . We consider five column densities of  $\log N_H [\text{cm}^{-2}] = 21, 21.5, 22.0, 22.5$ , and 23.0, and four metal abundance values: 1, 3, 5 and 10  $Z_\odot$ . Two metal enrichment schemes are considered: all metal abundances are scaled-up solar values, and metal enrichment in a starburst (Haman & Ferland 1997). We choose a typical AGN ionizing continuum (Korista et al. 1997). We examine the line ratio contours on the dual-parameter planes for the plausible regimes (an example of such contours is shown in Fig 7). We find that: (1) with

---

<sup>3</sup>Fe II forbidden transitions in this band is weak (Véron-Cetty et al. 2004 )

a solar and scaled solar metallicity, large Si III]/C III] $\sim 1$  can be reproduced only at a high density  $n_H > 10^{9.5} \text{ cm}^{-3}$  for the parameter ranges explored, while it can be produced in a wide parameter range for the starburst metallicity; (2) a large N III]/C III] ratio for C4 can only be reproduced at a large starburst metallicity  $Z > 12Z_\odot$ . At small column densities ( $\log N_H < 22$ ), the line ratio is high at a relative high ionization parameters; while at large column density, the line ratio is essentially independent of ionization parameters; (3) for C4, in the column density and density ranges considered here, N III]/N IV] suggests a low ionization parameter than C III]/C IV].

## REFERENCES

- Baldwin, J. A., Phillips, M. M., & Terlevich, R. 1981, PASP, 93, 5
- Baldwin, J. A., Hamann, F., Korista, K. T., Ferland, G. J., Dietrich, M., & Warner, C. 2003, ApJ, 583, 649
- Bechtold, J., Dobrzycki, A., Wilden, B., Morita, M., Scott, J., Dobrzycka, D., Tran, K.-V., & Aldcroft, T. L. 2002, ApJS, 140, 143
- Bianchi, S., Guainazzi, M., Matt, G., Chiaberge, M., Iwasawa, K., Fiore, F., & Maiolino, R. 2005, A&A, 442, 185
- Boroson, T. A., & Meyers, K. A. 1992, ApJ, 397, 442
- Boyce, P. J., et al. 1996, ApJ, 473, 760
- Calzetti, D., Armus, L., Bohlin, R. C., Kinney, A. L., Koornneef, J., & Storchi-Bergmann, T. 2000, ApJ, 533, 682
- Canalizo, G., & Stockton, A. 2000, AJ, 120, 1750
- Canalizo, G., & Stockton, A. 2000, ApJ, 528, 201
- Cao, C. et al., MNRAS, 390, 336
- Collins, N. R., Kraemer, S. B., Crenshaw, D. M., Bruhweiler, F. C., & Meléndez, M. 2009, ApJ, 694, 765
- Crenshaw, D.M., Kraemer S.B., & George I.M. 2003, ARA&A, 41, 117
- Das, V., et al. 2005, AJ, 130, 945



- Darling, J., & Giovanelli, R. 2002, *AJ*, 124, 100
- Di Matteo, T., Springel, V., & Hernquist, L. 2005, *Nature*, 433, 60
- Dwivedi, B. N., Mohan, A., & Gupta, A. K. 1995, *Sol. Phys.*, 161, 241
- Ferland, G. J., Korista, K. T., Verner, D. A., Ferguson, J. W., Kingdon, J. B., & Verner, E. M. 1998, *PASP*, 110, 761
- Gabel, J. R., et al. 2005, *ApJ*, 631, 741
- Hamann, F. 1997, *ApJS*, 109, 279
- Hao, C. N., Xia, X. Y., Mao, S., Wu, H., & Deng, Z. G. 2005, *ApJ*, 625, 78
- Hao, L., Weedman, D. W., Spoon, H. W. W., Marshall, J. A., Levenson, N. A., Elitzur, M., & Houck, J. R. 2007, *ApJ*, 655, L77
- Heckman, T. M., Kauffmann, G., Brinchmann, J., Charlot, S., Tremonti, C., & White, S. D. M. 2004, *ApJ*, 613, 109
- Ho, L. C. 2005, *ApJ*, 629, 680
- Hutchings, J. B., Crampton, D., Morris, S. L., Durand, D., & Steinbring, E. 1999, *AJ*, 117, 110
- Kewley, L. J., Groves, B., Kauffmann, G., & Heckman, T. 2006, *MNRAS*, 372, 961
- Kirhakos, S., Bahcall, J. N., Schneider, D. P., & Kristian, J. 1999, *ApJ*, 520, 67
- Komossa, S., Burwitz, V., Hasinger, G., Predehl, P., Kaastra, J. S., & Ikebe, Y. 2003, *ApJ*, 582, L15
- Kuraszkiewicz, J. K., et al. 2003, *ApJ*, 590, 128
- Laor, A., & Draine, B. T. 1993, *ApJ*, 402, 441
- Leitherer, C., et al. 1999, *ApJS*, 123, 3
- Lípari, S., Terlevich, R., Zheng, W., Garcia-Lorenzo, B., Sanchez, S. F., & Bergmann, M. 2005, *MNRAS*, 360, 416
- Lípari, S., Terlevich, R., Díaz, R. J., Taniguchi, Y., Zheng, W., Tsvetanov, Z., Carranza, G., & Dottori, H. 2003, *MNRAS*, 340, 289

- Lu, H., Zhou, H., Wang, J., Wang, T., Dong, X., Zhuang, Z., & Li, C. 2006, *AJ*, 131, 790
- Moshir, M., et al., 1990, in *IRAS Faint Source Catalog, —b—>10 Degree, Version 2.0*
- Nagao, T., Maiolino, R., & Marconi, A. 2006, *A&A*, 459, 85
- Netzer, H., & Laor, A. 1993, *ApJ*, 404, L51
- Astrophysics of gaseous nebulae and active galactic nuclei, 1989, *UN Iversity Science Books*
- Pasquali, A., Gallagher, J. S., & de Grijs, R. 2004, *A&A*, 415, 103
- Pettini, M., & Pagel, B. E. J. 2004, *MNRAS*, 348, L59
- Remillard, R. A., Bradt, H. V. D., Brissenden, R. J. V., Buckley, D. A. H., Roberts, W., Schwartz, D. A., Stroozas, B. A., & Tuohy, I. R. 1993, *AJ*, 105, 2079
- Richards, G. T., et al. 2006, *ApJS*, 166, 470
- Ruiz, J. R., Crenshaw, D. M., Kraemer, S. B., Bower, G. A., Gull, T. R., Hutchings, J. B., Kaiser, M. E., & Weistrop, D. 2005, *AJ*, 129, 73
- Rupke, D. S., Veilleux, S., & Sanders, D. B. 2005, *ApJ*, 632, 751
- Sanders, D. B., & Mirabel, I. F. 1996, *ARA&A*, 34, 749
- Schlegel, D. J., Finkbeiner, D. P., & Davis, M. 1998, *ApJ*, 500, 525
- Schweitzer, M., et al. 2006, *ArXiv Astrophysics e-prints*, arXiv:astro-ph/0606158
- Siebenmorgen, R., Freudling, W., Krügel, E., & Haas, M. 2004, *A&A*, 421, 129
- Skrutskie, M.F., et al., 2006, *AJ*, 131, 1163
- Springel, V., Di Matteo, T., & Hernquist, L. 2005, *ApJ*, 620, L79
- Sirocky, M. M., Levenson, N. A., Elitzur, M., Spoon, H. W. W., & Armus, L. 2008, *ApJ*, 678, 729
- Vanden Berk, D. E., et al. 2006, *AJ*, 131, 84
- Vázquez, G. A., & Leitherer, C. 2005, *ApJ*, 621, 695
- Véron-Cetty, M.-P., Joly, M., & Véron, P. 2004, *A&A*, 417, 515
- Weingartner, J. C., & Draine, B. T. 2001, *ApJ*, 548, 296

- Weedman, D. W., et al. 2005, *ApJ*, 633, 706
- Weymann, R. J., Morris, S. L., Foltz, C. B., & Hewett, P. C. 1991, *ApJ*, 373, 23
- Wu, H., Cao, C., Hao, C.-N., Liu, F.-S., Wang, J.-L., Xia, X.-Y., Deng, Z.-G., & Young, C. K.-S. 2005, *ApJ*, 632, L79
- York, D. G., et al. 2000, *AJ*, 120, 1579
- Zheng, Z., Wu, H., Mao, S., Xia, X.-Y., Deng, Z.-G., & Zou, Z.-L. 1999, *A&A*, 349, 735
- Zhou, H., Wang, T., Dong, X., Wang, J., & Lu, H. 2005, *Memorie della Societa Astronomica Italiana*, 76, 93 2285

Table 1. Center and width for each component

Component	$v$ km s <sup>-1</sup>	$\sigma$ km s <sup>-1</sup>
C1	-1 ± 8	183±7
C2	-357 ±26	257±18
C3	-82 ±79	933±59
C4	-1646±33	858±17

Table 2. Emission line strengths for each component<sup>1</sup>

Line	C1	C2	C3	C4
H $\alpha$	341±59	597±73	817±124	829±56
H $\beta$	55±10	50±12	160±26	198±19
H $\gamma$	8±7	11±8	112±49	77±15
[O III]5007	50±9	57±11	113±23	532±20
[O III]4959	17	19	38	213±12
[O III]4363	...	...	19±14	134±28
[O III]1663	...	...	120±31	100±29
[Ne III]3869	7±8	68±13	39±33	308±18
[N II]6584	295±20	52±36	...	...
[O I]6310	52±6	12±6	...	...
[O II]3727	294±17	96±15	...	...
[S II]6713	118±9	35±9	...	...
C IV1549	...	...	0	1403±41
C III]1909	...	...	564±45	196±63
N III]1750	...	...	91±27	751±32
Si III]1890	...	...	473±64	194±40
Al III]1860	...	...	63±11	55±11
N IV]1486	...	...	...	230±28

<sup>1</sup>in units of 10<sup>-17</sup> erg s<sup>-1</sup>cm<sup>-2</sup>

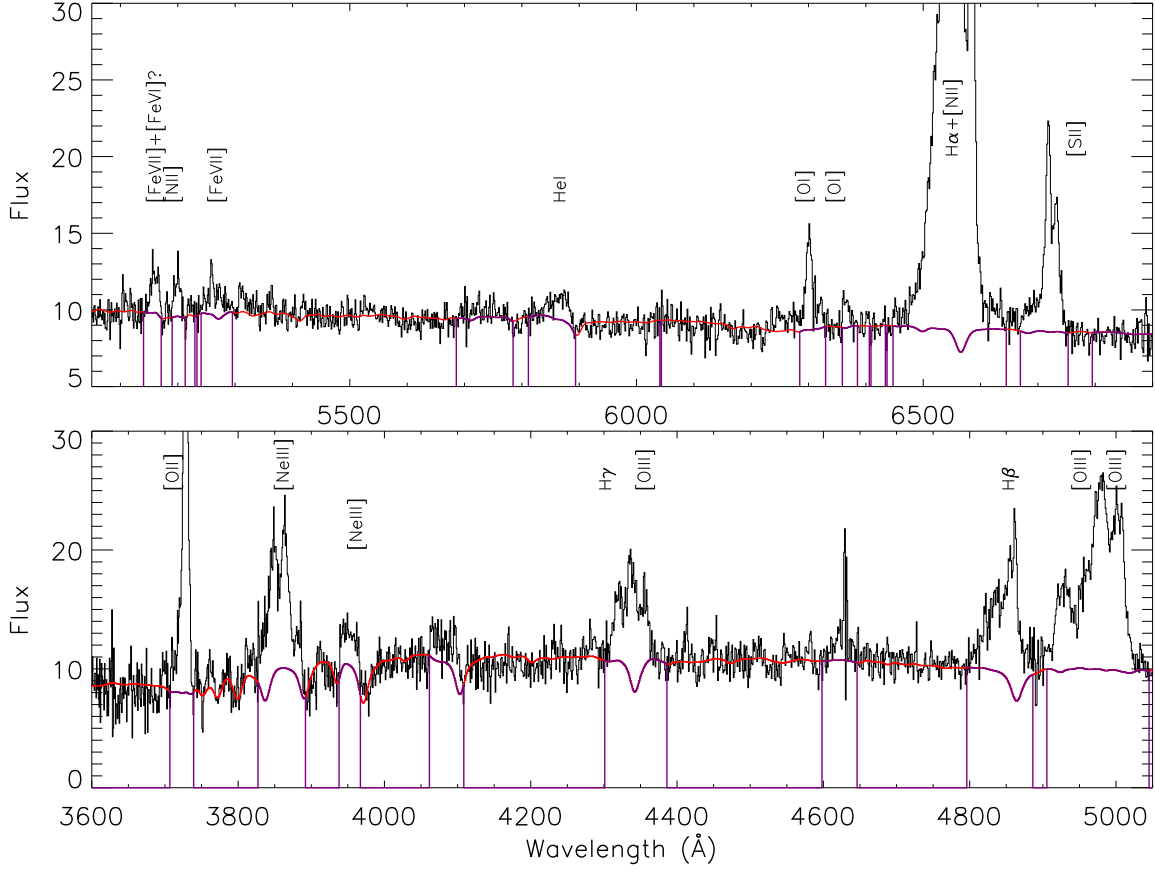
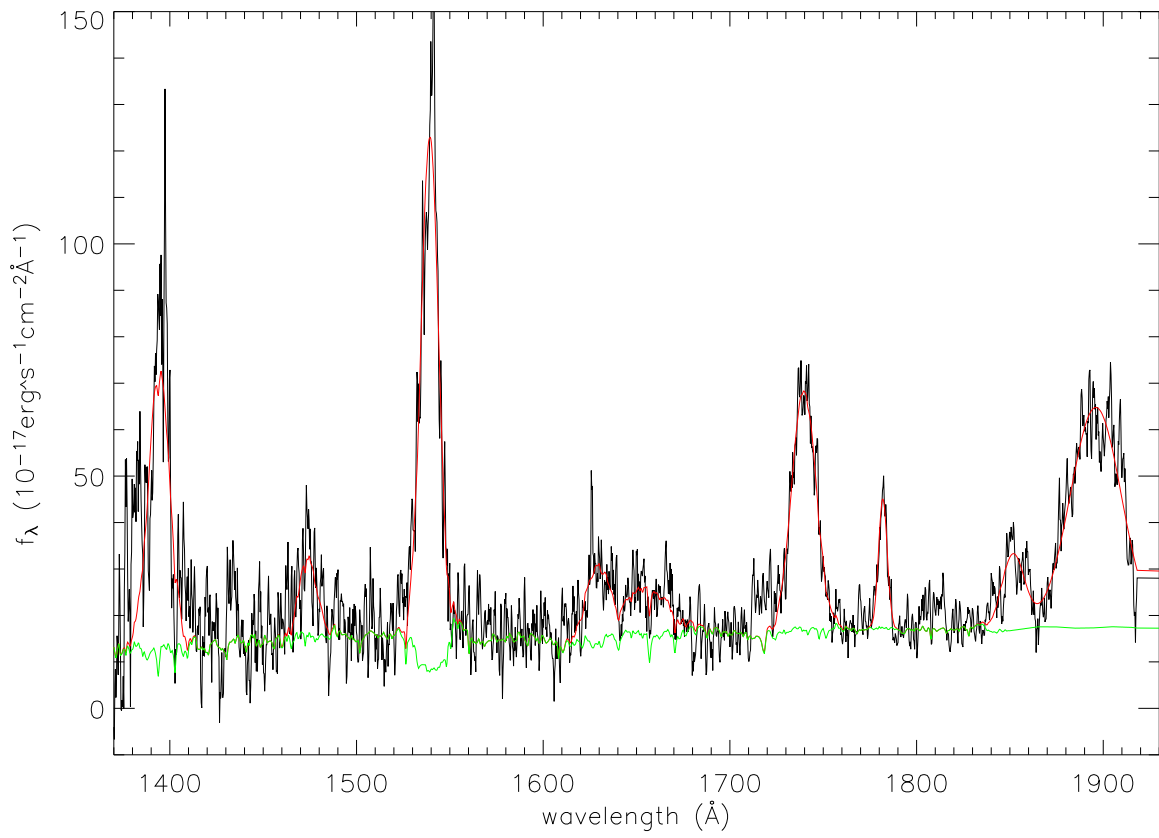
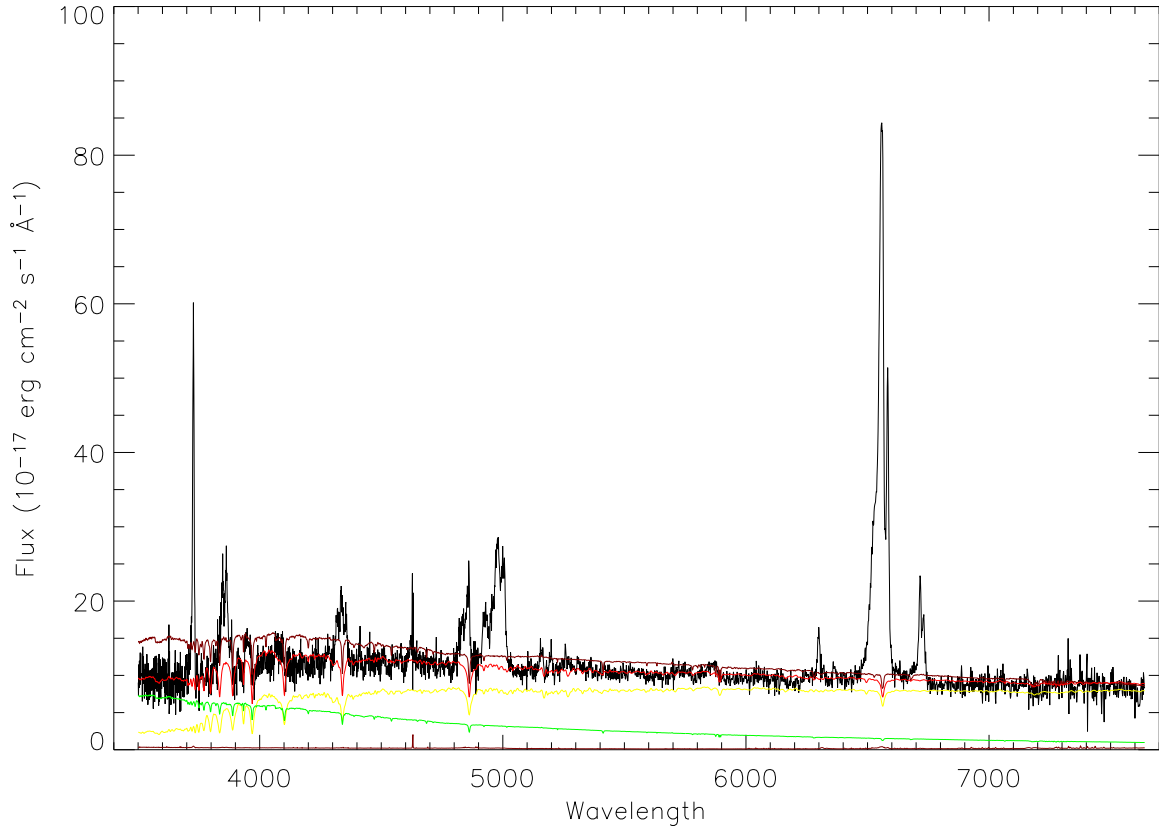
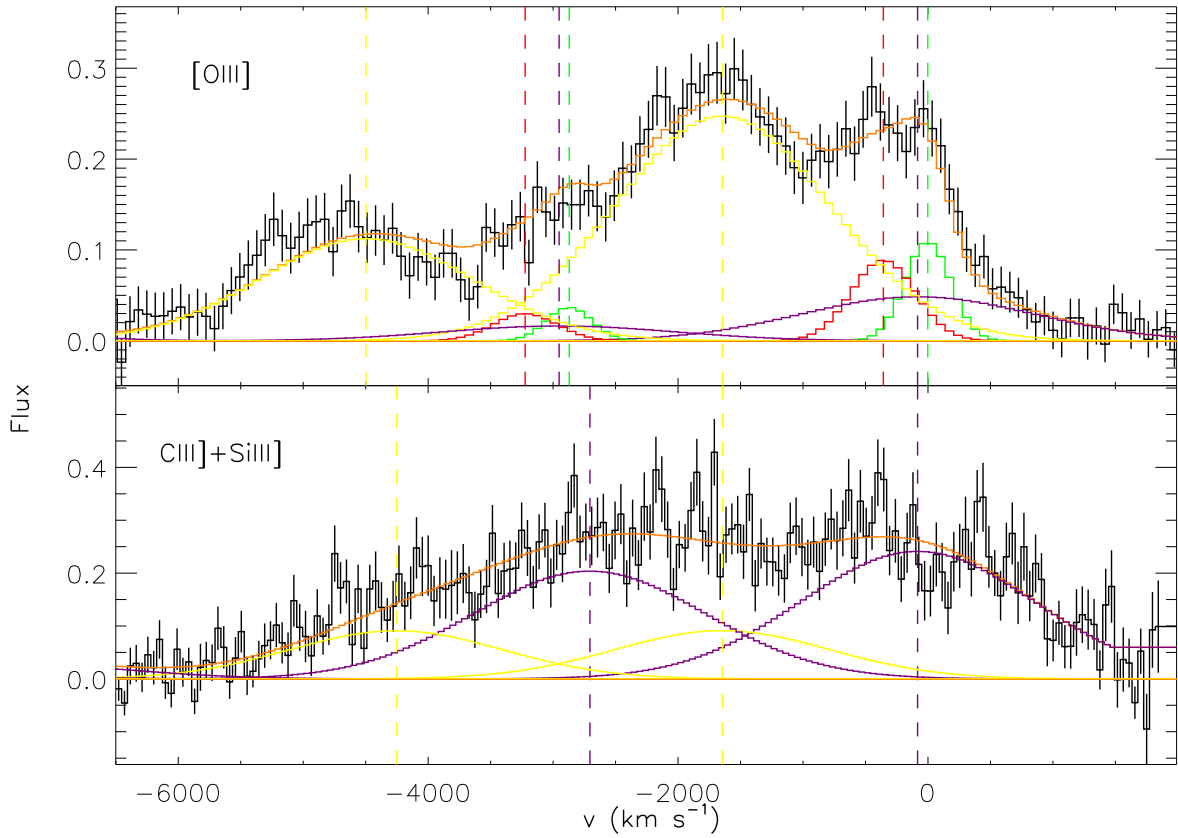
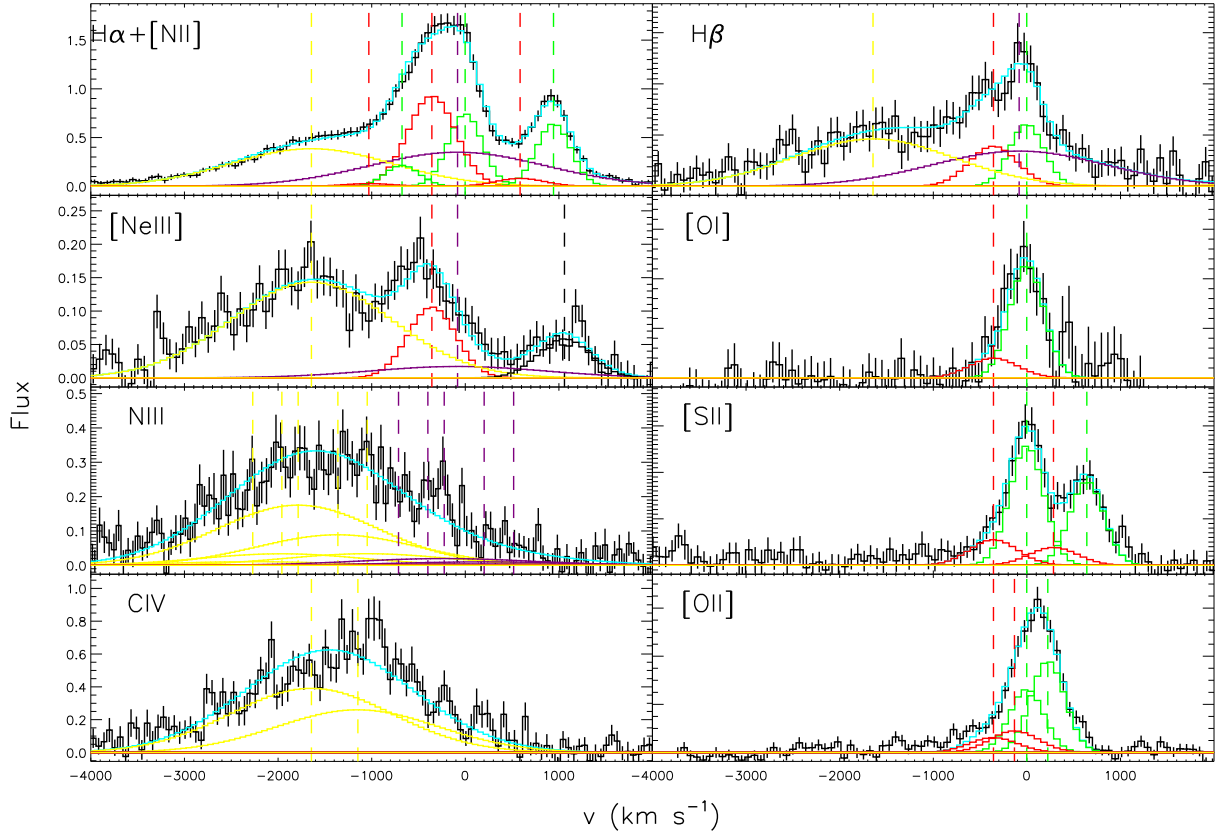


Fig. 1.— Optical (SDSS) spectrum of Q1321+058 and the best-fit star light model (see text for details). Prominent emission lines are labeled. Masked regions during the stellar light fit are marked in purple color.







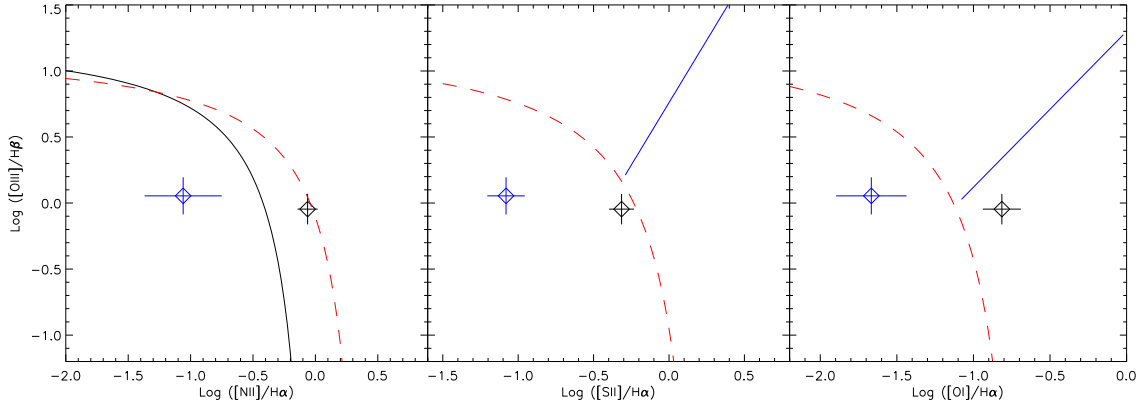


Fig. 4.— BPT diagrams for C1 (black diamonds) and C2 (blue diamonds). Black curve represents the empirical boundary separating star-forming galaxies from AGNs (Kauffmann et al. 2003), while red curves for the theoretical curve of extreme starburst (Kewley et al. 2001). The blue straight lines divide LINERs from Seyfert galaxies.

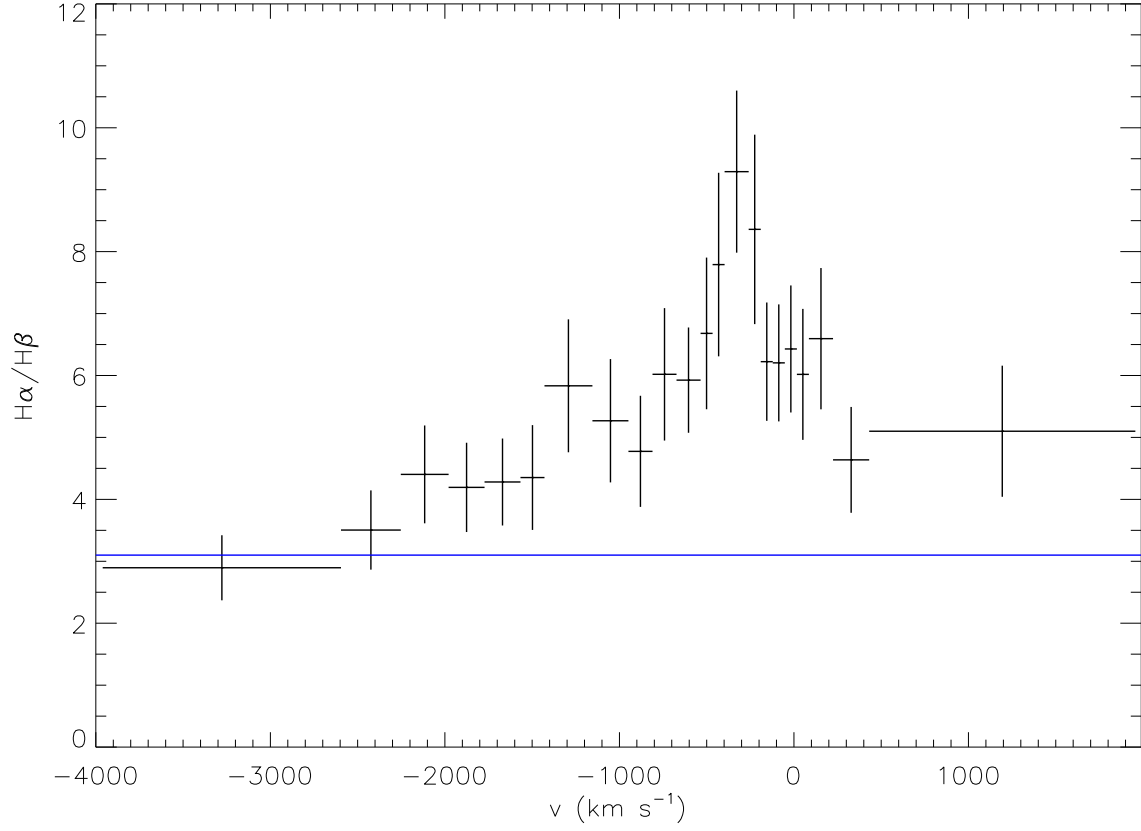


Fig. 5.— Wavelength-dependent  $\text{H}\alpha/\text{H}\beta$  ratio over the emission line profile. The best-fit [N II] model has been subtracted from the  $\text{H}\alpha$ + [N II] blend. It shows a clear peak at position of C2. The horizon line marks  $\text{H}\alpha/\text{H}\beta=3.1$ .

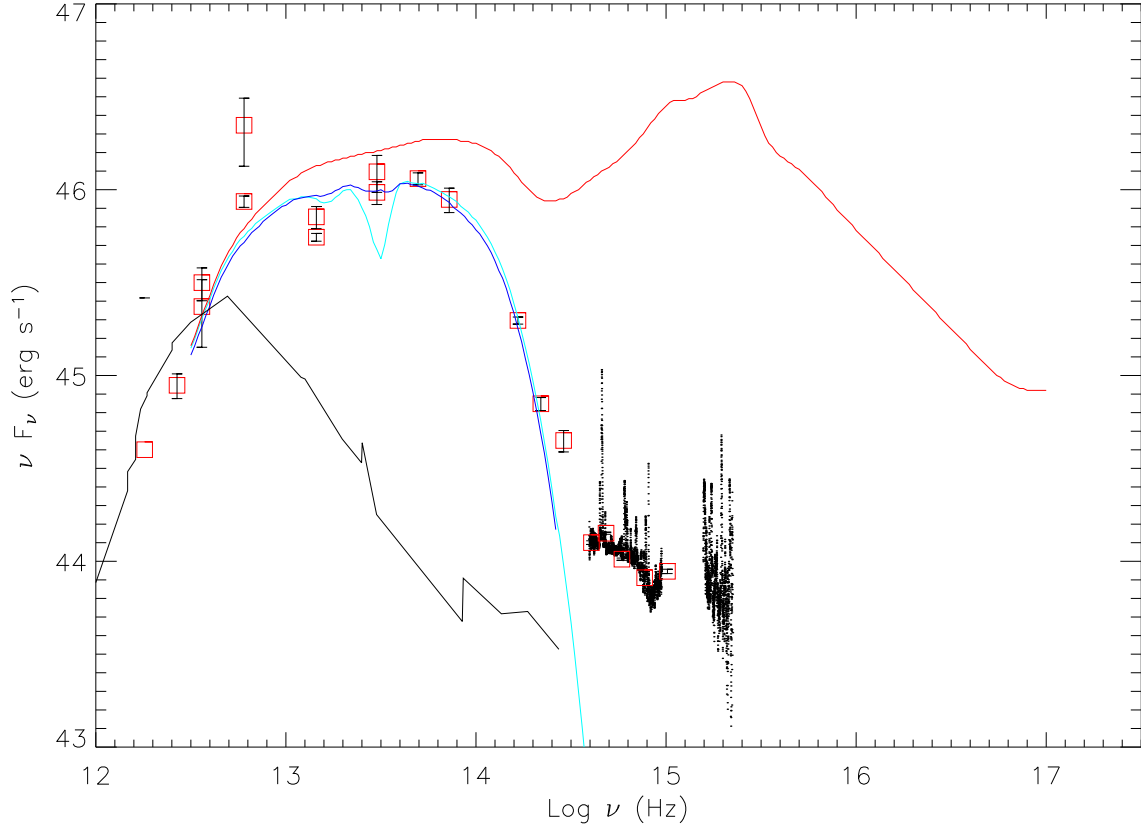


Fig. 6.— Spectral energy distribution from far-infrared to ultraviolet for Q1321+058. The infrared SED of NGC 6240 is shown in solid line, the template of infrared-luminous quasars in Richards et al. (2006) in red, while the quasar template reddened by  $E(B-V)=4.5$  in blue.

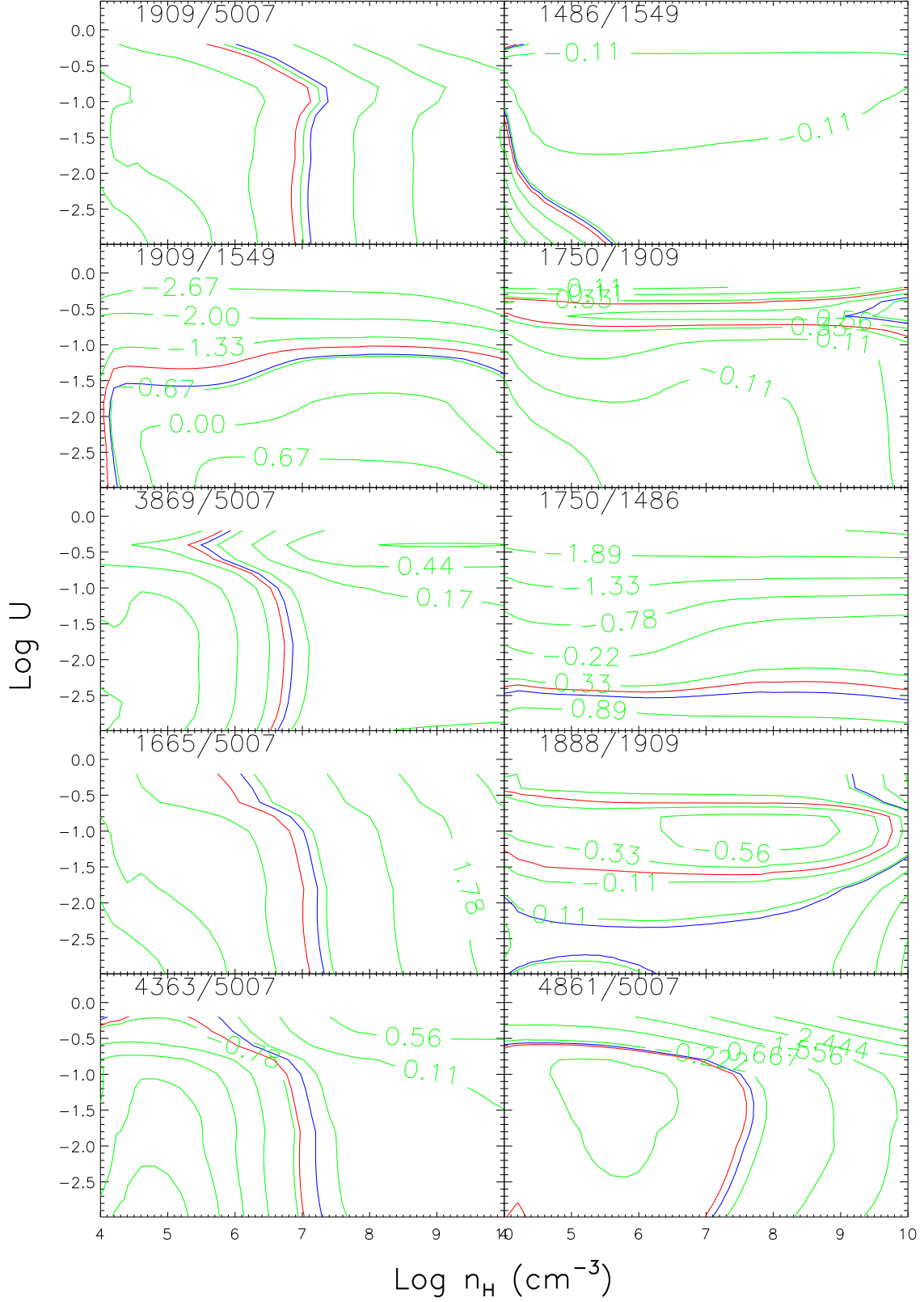


Fig. 7. Contours of emission line ratios in the ionization parameter – density space calculated using the photoionization code CLOUDY (Ferland et al. 1998).